

Multiscale Sampling Geometries and Methods for Deterministic and Stochastic Reconstructions of Magnitude and Phase Spectra of Satellite Imagery

Oliver Jeromin, *Member, IEEE*, and Marios S. Pattichis, *Senior Member, IEEE*

Abstract—This paper presents new methods for phase and magnitude interpolation and demonstrates their usefulness in reconstructing images from a limited number of frequency samples. A collection of multiscale frequency domain sampling geometries are developed based on the partition of the spectrum into low-, medium-, and high-frequency blocks. A nonstationary statistical approach is introduced that is based on adaptively selecting the best stochastic model in each frequency block. To develop effective models, the magnitude spectrum is preprocessed using a logarithmic transformation. Phase interpolation requires preprocessing by an appropriate phase unwrapping method. The new stochastic interpolation method is compared against cubic spline, bilinear, and nearest neighbor interpolation methods. Image reconstruction results are presented for sampling rates that retain 6.01% to 28.91% of the 2-D fast Fourier transform (FFT) samples. Image interpolation methods are compared based on the peak signal-to-noise ratio and the mean structural similarity index for satellite images of rural, natural, and urban images. The results indicate that the stochastic (Kriging) interpolation approach provides the best rural image reconstructions using just 6.01% of the 2-D FFT samples. Bilinear interpolation also gave excellent reconstructions for natural and urban images. For natural and urban images, stochastic interpolation gave the best magnitude-only interpolation results.

Index Terms—Magnitude spectrum interpolation, phase spectrum interpolation.

I. INTRODUCTION

A WIDE variety of remote sensing applications can benefit from effective frequency-domain interpolation methods. Potential applications range from image formation, super-resolution, and image compression. Just as important, while particularly challenging, is the development of new methods for phase spectrum interpolation (see [1] for the importance of phase for general signals). In remote sensing applications, the phase represents a physical measurement such as surface topography in interferometry [2]–[9]. Given the significant

differences between phase and magnitude spectra, we will consider them separately.

The study of frequency-domain image representations can be motivated from the basic image formation processes. As an example, in computed tomography (CT), imaging consists of sampling the spectrum along a collection of radial lines [10]. Image reconstruction requires interpolation from the radial line samples on a regular Cartesian frequency grid. CT images are then reconstructed using a regular 2-D (or 3-D) inverse-fast Fourier transform (FFT). A CT imaging formulation of spotlight-mode synthetic aperture radar can be found in [11]. Super-resolution methods can also be thought of as methods for recovering high-frequency information from lower frequency images [12]. A more general example is to simply consider image reconstructions from limited numbers of frequency-domain samples. In all of these applications, effective methods for frequency domain interpolation can lead to better reconstructions.

In CT, the standard frequency-domain interpolation methods are based on nearest neighbor and bilinear interpolation (page 59 in [10]). More generally, splines are recommended as “a perfect fit for signal and image processing” in [13], with spline interpolation as one of the best-known applications.

In what follows, we will consider the phase and magnitude spectrum interpolation separately. Here, note that the phase spectrum is well-known to be of fundamental importance for reconstructing both signals and images [1]. As shown in [1], under suitable conditions, objects of finite extent can be fully reconstructed from their phase-spectrum samples.

In this paper, our focus will be on the reconstruction of remote sensing imagery from magnitude and phase spectrum samples. The methods are developed and tested on ten representative and openly available satellite images of urban, rural, and natural scenery (see examples in Fig. 1). For testing our results, we have used three rural images, five urban images, and two natural images [14]–[17]. The urban images are selected subregions of a single, large ASTER SpectroRadiometer image of London, England.

Our primary focus is on the development of effective interpolation methods that can be used to reconstruct the original input images from a limited number of frequency domain samples. The basic approach can be summarized in three steps. First, the phase and magnitude spectral samples are generated using a 2-D FFT. Second, phase and magnitude interpolation is used to reconstruct the 2-D FFT spectrum from a limited subset of the original samples. Third, an approximation to the original image is obtained using an inverse 2-D FFT.

Manuscript received April 30, 2011; revised September 19, 2011 and January 11, 2012; accepted January 13, 2012. Date of publication February 27, 2012; date of current version September 21, 2012.

O. Jeromin is with Gentex Corporation, Zeeland, MI 49464 USA and also with the Sandia National Laboratories and the Department of Electrical and Computer Engineering, University of New Mexico, Albuquerque, NM 87131 USA (e-mail: oliver.jeromin@gentex.com).

M. S. Pattichis is with the Department of Electrical and Computer Engineering, University of New Mexico, Albuquerque, NM 87131 USA (e-mail: pattichis@ece.unm.edu).

Color versions of one or more of the figures in this paper are available online at <http://ieeexplore.ieee.org>.

Digital Object Identifier 10.1109/TGRS.2012.2185805

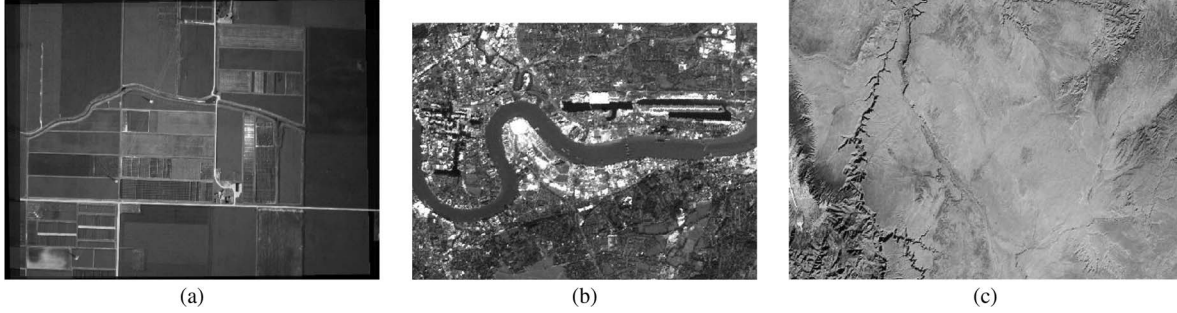


Fig. 1. Three of the ten images used in this study, sampled from the three image class types. (a) Purdue University Agronomy Research Center,¹ size 1069×1374 (rural example). (b) Sub scene from ASTER SpectroRadiometer image of London, England,² size 401×501 (urban example). (c) The Grand Canyon and surrounding country,³ size 351×501 (natural image example). The displayed images in (b) and (c) are subimages of all the images that are available at the web links. http://www.lars.purdue.edu/home/image_data/spectral_vision_data.html, Name: sv010813_ARC_F106_1m; <http://asterweb.jpl.nasa.gov/gallery/images/london-final.jpg>; <http://photojournal.jpl.nasa.gov/catalog/PIA03402>.

There are significant challenges associated with the sampling and interpolation processes. In summary, the primary ideas (and contributions) of this paper are as follows.

- *Multiscale frequency-domain sampling geometries*: A collection of sampling geometries is introduced that provides for dense sampling near the lower frequencies, followed by sparser sampling in the medium frequencies, and very sparse sampling in the higher frequencies. The motivation for the approach comes from the fact that the majority of image energy is concentrated in the lower frequency bands, with significantly less energy in the higher frequency bands. We use the term *multiscale* to describe the approach (see [18] for a similar frequency-domain partition). We consider independent sampling geometries for the phase and magnitude spectra, with denser sampling geometries reserved for the phase spectrum (motivated by [1]).
- *Nonstationary adaptive stochastic spectral modeling*: We introduce an adaptive approach that selects the best stochastic model based on the best fit from a collection of stochastic models. The approach is based on an extension of spatial statistical models and methods to the spectral domain [19]. Furthermore, the method does not assume stationarity over the entire spectral domain. Instead, stationarity is only assumed over selected partitions of the frequency spectrum.
- *Phase spectrum interpolation based on phase unwrapping*: Phase interpolation is very challenging due to significant phase-wrapping artifacts. This necessitates the use of phase unwrapping prior to stochastic modeling and interpolation. A collection of phase unwrapping algorithms are evaluated to select the best approach.
- *Magnitude spectrum interpolation based on logarithmic transformation*: Magnitude interpolation is complicated by the significant decay as a function of frequency magnitude. To address this issue, stochastic modeling requires the use of a logarithmic transformation prior to interpolation. As we describe in Section II, this transformation also allows us to provide effective stationary model approximations to nonstationary random fields. The basic three-step process is simply to 1) apply the $\log(\cdot)$ to the magnitude spectrum,

2) interpolate, and 3) apply the $\exp(\cdot)$ function to reconstruct the magnitude spectrum.

- *Quantitative comparisons of stochastic and deterministic approaches based on the mean structural similarity index*: To evaluate the effectiveness of the approach we provide quantitative reconstruction results based on the peak signal-to-noise ratio (PSNR) and the mean structural similarity (SSIM) index [20]. Here, we note that the use of the PSNR has been shown to correlate very poorly to human perception [21]. The mean SSIM provides for an objective assessment of the quality of the reconstructed images. SSIM is defined over local image windows at every pixel using

$$\text{SSIM}_{I,J}(i,j) = L_{I,J}(i,j) \cdot C_{I,J}(i,j) \cdot S_{I,J}(i,j)$$

where $L_{I,J}$ is a measure of local luminance similarity, $C_{I,J}$ is a measure of local contrast similarity, and $S_{I,J}$ is a measure of local structure similarity. They are given by

$$L_{I,J}(i,j) = \frac{2\mu_I(i,j) \cdot \mu_J(i,j) + C_1}{\mu_I^2(i,j) + \mu_J^2(i,j) + C_1},$$

$$C_{I,J}(i,j) = \frac{2\sigma_I(i,j) \cdot \sigma_J(i,j) + C_2}{\sigma_I^2(i,j) + \sigma_J^2(i,j) + C_2},$$

$$S_{I,J}(i,j) = \frac{2\sigma_{I,J}(i,j) + C_3}{\sigma_I(i,j) \cdot \sigma_J(i,j) + C_3}$$

where μ_I, μ_J denote the weighted averages, σ_I, σ_J denote the weighted standard deviations, $\sigma_{I,J}$ denotes the cross-standard deviation, and C_1, C_2, C_3 are stabilizing constants. The mean SSIM is the average SSIM over the entire image region. The PSNR and mean SSIM measurements are used to compare the proposed stochastic approach with the nearest neighbor, bilinear, and cubic interpolation methods. Separate comparisons are provided for rural, natural, and urban images.

The proposed stochastic method for phase and magnitude spectrum interpolation is termed Kriging by Matheron [22]. According to [22], Kriging was independently developed by Matheron and Gandin. In what follows, we provide a brief summary of Kriging applications in remote sensing.

Cheng *et al.* used Kriging to interpolate terrain elevation information to rectify SPOT satellite images in [23]. Kanaroglou *et al.* [24] used Kriging to estimate the missing pollution map levels when ground cover and clouds obstruct measurement. Rossi *et al.* [25] used Indicator Kriging to interpolate unknown image regions of Landsat Thematic Mapper images. Ferretti *et al.* utilized Kriging to filter and resample the atmospheric permanent scatterers that influence the accuracy of synthetic aperture radar (SAR) interferometry [26]. Blaschke utilized Kriging for object classification in remotely sensed images to assist in appending a geographic information system database to the image data [27]. Djamdji and Bijaoui [28] utilized Kriging to map the disparities over two stereo images. The disparity map was then used to register the two images that constitute the pair. Carr demonstrated that Kriging can be modeled in a way to achieve less smoothing in Kriging by performing a two-step Kriging process, where the outputs are combined in a way that is analogous to summing high- and low-pass filtered images [29].

More recently, Atkinson *et al.* used cokriging based on coregistered images of different spatial and spectral resolutions to provide reconstructions at increased spatial resolution (super-resolution) [30]. Foster and Evans [31] reported on the use of Kriging and other methods for reconstructing ionospheric total electron count maps. In [32], the authors showed that Kriging methods are very effective in providing regional objective analysis for merging several data sets.

In our approach, we consider the application of Kriging methods for reconstructing the full Fourier spectrum from a dyadic, multiscale sampling of the frequency domain. The motivation for choosing this frequency grid comes from the desire to produce effective image reconstructions at relatively low sampling densities. In other words, our motivation comes from developing an effective approach for representing and encoding remote sensing imagery. By keeping the sampling density low, we have an effective image compression approach. Here, we note that effective methods for remote sensing image compression are of current interest (see [33]–[36]).

As in our paper, the authors in [33]–[35] were interested in developing fast methods for coding remote sensing images. The authors in [33] presented a low-complexity method for lossless compression of hyperspectral images by using joint decoding of correlated bands of hyperspectral images. Similarly, in [34], the authors presented a modification of the Karhunen–Love transform (KLT) to allow for a fast method for coding remote-sensing images. In [35], the authors propose a pairwise orthogonal transform for spectral image coding that is recommended as a spectral decorrelator that is more efficient than wavelets without having the high computational complexity associated with the KLT.

Our basic idea of reconstructing images from a limited number of frequency-domain samples is also related to compressive sensing approaches. Here, we note that the authors of [36] proposed the use of compressive sensing techniques for space-time tomographic SAR inversion. This approach provided a method of spatial-time interpolation that is motivated from the fact that tomographic elevation resolution is sampled at “at least one order of magnitude lower than in range and azimuth” [36].

Our approach of minimizing the required number of FFT coefficients has both direct and indirect applications in remote sensing. Directly, our approach allows us to effectively compress the image. Here, a fraction of the FFT coefficients need to be transmitted. The images can then be reconstructed from limited frequency-domain samples. An indirect application comes from the fact that we can achieve significant computational savings based on the fact that frequency-domain interpolation from the acquisition geometry to the FFT sampling geometry (for image formation) only needs to reconstruct a small fraction of the full-scale FFT-grid samples. Another indirect application comes from the possible redesign of the (frequency-domain) image acquisition geometry to only produce samples that are close to the reduced number of FFT samples required by the multiscale geometry. Here, note that the standard method for addressing the relationship between the imaging acquisition geometry is to provide some guarantee of the resulting image resolution (e.g., see [37]). In our approach here, starting from an image reconstructed at a given resolution, we show how to reduce the number of frequency-domain samples to achieve image reconstruction of sufficient image quality. When the image acquisition is in the frequency domain, as in SAR, this information can be used to select an acquisition geometry with frequency sampling densities that are at least as dense as the geometries discussed here. While we do not pursue this application in this paper, this indirect application of our research appears to be relatively straightforward.

Given our target image encoding application, it is also interesting to ask why we did not consider spatial-domain Kriging as an alternative. To address this, note that spatial-domain methods do not have the indirect effect of controlling the sampling density of FFT frequencies that need to be interpolated. Furthermore, as we shall see in the results section, a very fast and effective frequency-domain method based on Ordinary Kriging (OK) can be used to provide effective interpolation in the frequency domain. On the other hand, while the stochastic models may be simpler, our approach does require phase unwrapping.

We also note that the use of a predefined sampling geometry allows us to investigate image compression methods that do not require the overhead associated with having to encode the spectral location of the FFT coefficients. Thus, our approach also avoids having to store the coefficient number as required by popular methods such as basis pursuit [38]. The rest of the paper is organized as follows. A theoretical background of the spectral statistical models is given in Section II. This is followed by a detailed description of the methodology in Section III. The results are provided in Section IV, followed by concluding remarks in Section V.

II. THEORETICAL BACKGROUND

A. Spectral Statistical Models

Digital images are characterized by a discrete spectrum that is periodic, with a fundamental 2-D frequency support from $-\pi$ to π in each dimension. The 2-D FFT of an image produces a discrete lattice of regularly spaced frequency samples over the continuous interval of $[-\pi, \pi]^2$. Here, we would like to investigate the use of methods from spatial statistics that allow

us to interpolate the 2-D FFT frequencies from a limited subset of these samples.

To fix the notation, we let the discrete frequency spectrum samples be at digital frequencies $\mathbf{s}_i = (u_i, v_i)$ where i is used for indexing the different samples. In this notation, the horizontal frequency coordinate is denoted by u_i , while v_i refers to the vertical frequency coordinate. Let $Z(\mathbf{s}_i)$ denote the phase or magnitude values sampled at location \mathbf{s}_i . The second-order stationary variogram is [19]

$$2\gamma(\mathbf{s}_1 - \mathbf{s}_2) = \text{var}(Z(\mathbf{s}_1) - Z(\mathbf{s}_2)) \quad (1)$$

where $\gamma(\cdot)$ denotes the semivariogram (half of the variogram).

Assuming an intrinsically stationary random field, the method of moments estimator, commonly referred to as the *classical* variogram estimator, is given by

$$2\hat{\gamma}(\mathbf{h}) \equiv \frac{1}{|N(\mathbf{h})|} \sum_{(i,j) \in N(\mathbf{h})} (Z(\mathbf{s}_i) - Z(\mathbf{s}_j))^2 \quad (2)$$

where $N(\mathbf{h})$ is defined by $N(\mathbf{h}) \equiv \{(i, j) : \mathbf{s}_i - \mathbf{s}_j = \mathbf{h}\}$ and $|N(\mathbf{h})|$ is the number of elements in the set $N(\mathbf{h})$. The classical estimator is **unbiased** but *not robust*. Here, we use the term robust with reference to contamination by outliers [19]. In other words, the presence of outliers can cause (2) to produce incorrect estimates.

Due to the periodic nature of the 2-D FFT domain, intrinsic stationarity cannot be assumed over the entire spectrum. In order to have confidence in our variogram estimates, we seek a partitioned spectral domain that lends itself to independent spectral statistical modeling within the regions defined by the partition. We intentionally select a dyadic partition, which allows us to explore our spectral models using a scalable framework. The dyadic partitioning results in outer regions that are four times as large as the next smaller regions (see Fig. 2). These high-frequency regions contain less spectral energy. Compared to the low-frequency bands, the higher frequency bands are sampled at a lower sampling density. Conversely, the innermost contain the low-frequency information of the image, and we want to preserve the original spectral content therein. Fig. 2 shows the half-spectrum partitions and numbers them for reference throughout this work.

For each spectral region, we first consider isotropic models to fit each magnitude and phase spectra empirical variograms with one of the following three theoretical semivariogram models [19].

- The Spherical Model:

$$\gamma(\mathbf{h}) = \begin{cases} 0, & \mathbf{h} = 0, \\ \sigma + \alpha \left\{ \frac{3}{2} (\|\mathbf{h}\|/\beta) - (\frac{1}{2} (\|\mathbf{h}\|/\beta)^3) \right\}, & 0 < \|\mathbf{h}\| \leq \beta \\ \alpha + \sigma, & \|\mathbf{h}\| > \beta, \end{cases} \quad \sigma \geq 0, \quad \alpha \geq 0, \quad \text{and} \quad \beta \geq 0. \quad (5)$$

- The Exponential Model:

$$\gamma(\mathbf{h}) = \begin{cases} 0, & \mathbf{h} = 0, \\ \sigma + \alpha \{1 - \exp(-\|\mathbf{h}\|/\beta)\}, & \mathbf{h} \neq 0, \end{cases} \quad \sigma \geq 0, \quad \alpha \geq 0, \quad \text{and} \quad \beta \geq 0. \quad (6)$$

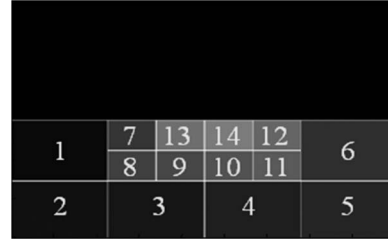


Fig. 2. Spectral partition map. The (zero-centered) discrete frequency domain is partitioned into high-frequency blocks (blocks 1–6), medium-frequency blocks (7–12), and low-frequency blocks (13, 14). The low-frequency blocks were sampled at the regular discrete Fourier transform (DFT) sampling rate. In this example, the DFT sampling grid is 301×401 , which is the same as the size of the original input image. The high-frequency blocks contain 75×112 samples while the low and medium-frequency blocks (7–15) contain 37×56 samples. Since we are dealing with real-valued images, the frequency spectrum is conjugate symmetric. Thus, we only need to work with two quadrants of the discrete frequency space. The other two quadrants are inferred by symmetry (see more details in Section III, the Methods section).

- The Gaussian Model:

$$\gamma(\mathbf{h}) = \begin{cases} 0, & \mathbf{h} = 0, \\ \sigma + \alpha \{1 - \exp(-(\|\mathbf{h}\|^2/\beta^2))\}, & \|\mathbf{h}\| \neq 0, \end{cases} \quad \sigma \geq 0, \quad \alpha \geq 0, \quad \text{and} \quad \beta \geq 0. \quad (7)$$

In the above models, σ is the nugget effect, which was termed by Matheron as a representation of small scale variations (in our case, subspectral sample variations) that manifest themselves as a discontinuity at the minimum measurable range value. The parameter α is referred to as the variogram sill, and it is defined as the limit of the variogram as the distance between samples approaches infinity. Typically, a good initial estimate for the variogram sill is the sample variance. Finally, β is referred to as the variogram range and can be thought of as the lag at which $Z(\mathbf{s})$ and $Z(\mathbf{s} + \mathbf{h})$ are no longer correlated. It can be used a guide to determining the lag distances required to include in spatial prediction.

General anisotropic models that can capture spatial correlations at all possible directions are impractical since they require estimation of 1-D variograms along a large number of directions. We would then need to select samples along each possible direction and range. For practical purposes, a simplified directional model is considered (e.g., see [39]). In the simplified model, anisotropic semivariograms are assumed to follow an ellipsoidal shape. Then, the application of the simplified model requires the determination of the principal variogram direction and the anisotropic ratio. Here, the principal direction and anisotropic ratio are defined in terms of the distance of maximum spatial correlation. Furthermore, the direction of minimum correlation is assumed to be orthogonal to the principal direction. To address the sampling issue, a tolerance parameter is used in order to provide the maximum allowed angle deviation. Unfortunately, in our case, the number of samples is also limited by the dyadic partitioning. Here, note that there are far fewer low-frequency samples than higher frequency available for model estimation. For determining anisotropic behavior, we consider Kriging directions every 15° . We provide an example in the results section.

Isotropic models turn to be robust due to the limited number of parameters that need to be estimated. In this case, only three

parameters are required. As such, they can be fitted to spectral regions with relatively small numbers of samples. On the other hand, the use of a simplified anisotropic model requires additional optimization to determine the principal direction over all possible cases.

B. Magnitude Spectrum Transformation for Stationary Random Field Approximation Over Fixed Regions

The magnitude spectrum can decay significantly as function of the discrete frequency magnitude. Here, the application of the stochastic models requires that we can provide a stationary random field approximation within each spectral region. However, within each spectral region, the fact that the magnitude spectrum can vary significantly leads us to consider a logarithmic transformation and trend removal. On the other hand, in general, we note that the application of the logarithmic transformation cannot be assumed to transform a nonstationary random process into a stationary one. We provide more formal details of our approach in this section.

When a given spectral-domain region violates the stationarity assumptions, it may be reasonable to expect that we can provide good, stationary approximations over a disjoint partition of subregions of the original region [19, p. 64]. Furthermore, instead of requiring stationarity over the original region, it is reasonable to assume that the **relative variogram**, defined by

$$2\gamma_Z^{(j)}(\mathbf{h})/\mu_j^2 \quad (8)$$

where μ_j denotes the j th subregion average, will remain approximately constant over all sub regions, independent of j . It can be shown that the application of the logarithmic transformation will produce an approximately intrinsically stationary random field over the original region [19]. The importance of this result is that the logarithmic transformation allows us to apply our methods over each spectral region of Fig. 2, without requiring any knowledge of the specific boundaries of the constituent subregions.

C. Phase Unwrapping

Phase interpolation presents significant challenges due to the fact that the estimated phase is wrapped into the interval $(-\pi, \pi]$. Sharp discontinuities in the wrapped phase make it particularly challenging for interpolation. On the other hand, phase unwrapping can generate large phase values which can magnify interpolation errors. To see this, note that a small phase reconstruction error for large values can map to a relatively large error in the wrapped interval of $(-\pi, \pi]$, and it is this wrapped interval that is relevant for reconstruction purposes.

We explored the use of five different 2-D phase unwrapping techniques that are described and implemented in software [40]. Three of the algorithms we applied to the phase spectra are path following techniques: Goldstein's Branch Cut method [3], quality guided path following [41], and Flynn's minimum discontinuity method [42]. The other two methods can be described as minimum norm methods, which approach phase unwrapping in a mathematically formal manner. These are the

preconditioned conjugate gradient (PCG) algorithm and the weighted multigrid algorithm (see [40]).

The minimum norm methods produce the smoothest surfaces but result in a very large range of unwrapped values. As mentioned earlier, large phase values are undesirable because the quality of the reconstructed phase depends on the relative error within the range of $(-\pi, \pi]$, regardless of the unwrapping method. Larger unwrapped phase values resulted in significant relative error within the range of $(-\pi, \pi]$ of the interpolated phase values. Unwrapped phase surfaces with the smallest range of values obtained by Flynn's minimum discontinuity method gave the best results.

D. Optimal Interpolation Using Kriging

Assuming that each spectral location can be modeled by the constant mean and zero-mean intrinsically stationary random process $\delta(\mathbf{s})$, we write $Z(\mathbf{s}) = \mu + \delta(\mathbf{s})$. OK estimates the optimal linear predictor using a weighted sum of the known data points within a region, \mathbf{B} using [19]

$$p(\mathbf{Z}; \mathbf{B}) = \sum_{i=1}^n \lambda_i Z(\mathbf{s}_i). \quad (9)$$

We also require that the optimal data points should satisfy

$$\sum_{i=1}^n \lambda_i = 1 \quad (10)$$

which guarantees uniform unbiasedness.

Numerical optimization techniques are used to minimize the prediction error with respect to the selected model values $(\lambda_1, \lambda_2, \dots, \lambda_n)$ and the resulting Lagrange multiplier that ensures the constraint holds resulting in a system of linear equations. The computational complexity of the Kriging interpolation step is dependent on the size of the linear system. In matrix form, the solution's computational complexity is governed by a matrix inversion of size $(N + 1) \times (N + 1)$, where N is the number of interpolated samples being sought.

For modeling possible trends in the data, we also consider Universal Kriging model of the form [19]

$$p(\mathbf{Z}; \mathbf{B}) = \sum_{j=1}^{p+1} \beta_{j-1} f_{j-1}(\mathbf{s}) + \delta(\mathbf{s}) \quad (11)$$

where $f_{j-1}(\mathbf{s}_i)$ is the j th function of position ($j = 1, 2, \dots, p + 1$), β is an unknown vector of $p + 1$ parameters, and $\delta(\mathbf{s})$ denotes a zero-mean intrinsically stationary random process. Here, note that the use of Universal model requires a choice of suitable trends functions and the estimation of the function coefficients (β).

III. METHODS

A. System Block Diagram

The overall system is summarized in Figs. 3 and 4. Fig. 3 summarizes the "encoding steps." In other words, it provides the phase and magnitude samples and the statistical model parameters that are needed for representing the input image.

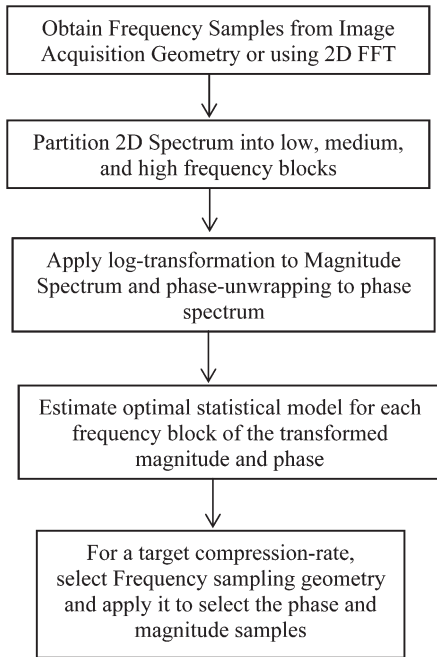


Fig. 3. Spectral sampling for remote sensing image compression. This represents the *encoder* part of the method. It produces the samples and the statistical model parameters that are needed for reconstruction. Refer to Table I for the target compression rates that can be achieved with the proposed approach.

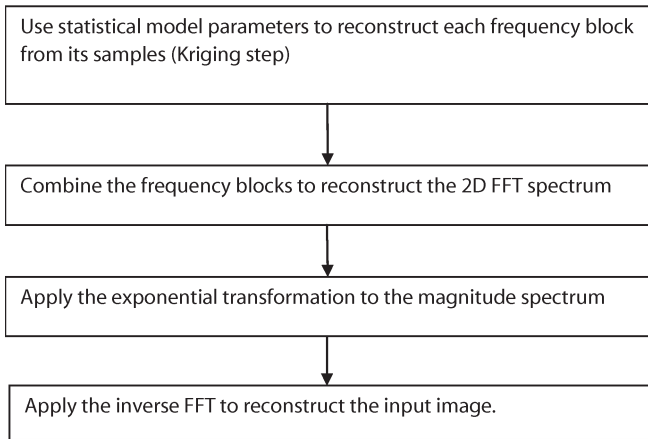


Fig. 4. Fourier and spatial image reconstruction flow chart. This represents the *decoder* part of the method. It represents the spatial image reconstruction procedure using only the statistical model parameters and the retained image and phase samples.

The “decoding steps” are given in Fig. 4. Fig. 4 provides the steps for reconstructing the input image from the retained spectral samples.

The encoding approach starts with selecting the target compression ratio based on the fraction of frequency-samples that will be retained. Given a target compression ratio from 6.01% to 28.91%, Table I can be used to select the best sampling geometry.

In the encoding phase, the phase and magnitude samples are obtained using a 2-D FFT. The frequency samples are partitioned into low, medium, and high-frequency blocks as given in Fig. 2. Prior to interpolation, the logarithmic transformation is applied to the magnitude spectrum. As discussed in Section II-D, phase unwrapping is performed using Flynn’s

minimum discontinuity method. The best statistical models are selected for each frequency block. The collection of the retained samples and the statistical models can be used for reconstruction as shown in Fig. 4.

In Fig. 4, the first step is to interpolate the phase and magnitude samples over each frequency block. The frequency block reconstructions are put together to reconstruct the 2-D FFT samples. The $\exp(\cdot)$ transformation is applied to the magnitude spectrum to invert the $\log(\cdot)$ step. The inverse 2-D FFT is then used to reconstruct the input image.

Here, note that for real images, only two quadrant samples are needed. The other two quadrants are obtained by conjugate symmetry. We will next provide more details on the sampling geometries, the interpolation process, the statistical model fitting, and the interpolation process.

B. Spectral Sampling Geometries

The scalable, adaptive spectral lattice sampling approach we propose allows for the use of the region-based spatial statistical models described above. First, utilizing the symmetry provide by the Fourier transform of real-valued data, $F(u, v) = F^*(-u, -v)$, where F^* is the complex conjugate operation, the magnitude spectra and phase spectra symmetry are expressed as $|F(u, v)| = |F(-u, -v)|$ and $\angle F(u, v) = -\angle F(-u, -v)$, respectively. This allows us to represent an $N \times N$ image by $(N/2 + 1) * N$ spectral samples. For implementing the phase unwrapping methods, we first reconstructed the phase over the entire frequency spectrum. Then, we take the real part of the reconstructed image.

We applied different uniformly spaced sampling rates for the large and small (outer and inner) dyadic partitions in a manner that reduced the number of frequency samples as a function of the relative frequency magnitude. In other words, the samples near the low-frequency components were not downsampled, as the majority of the image energy is concentrated there. Given that image energy drops with the increasing frequency magnitude, we considered sampling rate reductions for the outer and inner (non-dc) spectral partitions that are twice as dense for the blocks closer to the center of the spectrum. This allows analysis of sampling rate reductions for the outer and inner spectral partitions that provide acceptable image reconstructions. Table I summarizes the overall spectral sampling rate we achieve when uniformly sampling the magnitude and phase spectral regions at various rates. It is also important to note that we have independent sampling rates for frequency and phase samples. In all cases, the sampling geometries of the magnitude spectrum are a proper subset of the sampling geometries of the phase spectrum. This means that we have far less magnitude spectrum samples than phase spectrum samples. Furthermore, for each phase spectrum sample, we have the corresponding magnitude spectrum sample. This is due to the fact that phase interpolation is far more challenging than magnitude spectrum interpolation.

C. Variogram Model Selection and Fitting

First, we need to estimate three variables when selecting the appropriate model for the empirical variograms calculated within each frequency block. The second consideration

TABLE I
SPECTRAL STATISTICAL DATA SAMPLE RATES

PHASE SAMPLING RATE \ MAGNITUDE SAMPLING RATE	1:4/1:16	1:16/1:64	1:64/1:256
NONE: 1:1/1:1	S1: 28.91%	S2: 27.15%	S3: 26.71%
1:1/1:4	S4: 25.78%	S5: 24.02%	S6: 23.58%
1:4/1:16	S7: 11.72%	S8: 9.96%	S9: 9.52%
1:16/1:64	S10: 8.20%	S11: 6.45%	S12: 6.01%

required when calculating variogram models is the extent of the range that will be used in the variogram estimation. The additional computational cost of variogram calculation over the entire frequency block was chosen as part of the variogram estimation process. This ensures that our method is scalable; allowing multiple sampling rates within a single frequency partition to be explored based a single estimate of the variogram. In other words, we ensure that the estimated model provides a semivariance for the minimum sampling rate.

A third consideration that is explored is the number of semi-variance values to fit and which model best fits the empirical data. We appeal to numerical optimization to determine which model via nonlinear least squares curve fitting. The sampling rate applied to each spectral partition will be used to govern the size of the maximum lag we wish to fit the model to.

The consideration of anisotropic models requires the estimation of the dominant direction and the anisotropy ratio. Here, note that if the anisotropic model gives a ratio that is in the range of 0.7–1.0, we reject the anisotropic model in favor of an isotropic model. This avoids possible overfitting of isotropic data with an anisotropic model. Also, if the anisotropic model fits fail, we default to an isotropic model that tends to be more robust.

D. Kriging Interpolation of Magnitude and Phase Spectra

Both Ordinary and Universal Kriging are considered with the log-magnitude and unwrapped phase data. Two parameters were explored in finding the optimal Kriging result: the *max-distance* and the *max-samples* values. The former refers to the circular radius of the maximum discrete-frequency space distance that needs to be considered for estimating the missing value, while the latter refers to the exact maximum number of known FFT samples that need to be considered for providing the optimal estimate. We chose to limit our exploration to the *max-samples* parameter, as it is not prone to geometric constraints along the edges of the frequency blocks and provides consistent reconstruction models. Here, we note that the two are closely related. Based on the sampling geometry, we can derive the *max-samples* parameter from the *max-distance* parameter. Furthermore, it is clear that the *max-distance* parameter is closely related to the correlation length.

Using the *max-samples* value that provides the best reconstruction (in terms of PSNR), we reconstructed both the

magnitude and the unwrapped phase (using Flynn’s minimum discontinuity method) from variogram estimates calculated over all samples within a given spectral block. We compared both the reconstructed magnitude and phase samples from the Kriging method here to the established methods for 2-D interpolation: nearest-neighbor, bilinear, and spline interpolation. A comparison of the image produced by the inverse Fourier transform of all reconstructed spectral samples is also included, where the PSNR and SSIM matrix [20] are used to quantify the reconstructed spatial images.

IV. RESULTS

We summarize the results in four sections. First, we present results from nonstationarity tests on the magnitude. Second, we present results from the use of different variogram models. Then, we discuss interpolation results (Kriging), followed by comparisons of image reconstructions obtained by different methods.

A. Log-Magnitude Stationarity Assumption

A basic assumption of our model is that the use of the $\log(\cdot)$ operation results in a stationary model for the magnitude spectrum. Exploratory analysis of several spectral blocks did not show any significant trends or deviations from stationarity. The important exception to this observation comes from highly directional structures (e.g., images of roads). In such cases, small portions of the magnitude spectrum showed strong directional information. Thankfully, because a small portion of the spectrum is affected, our methods still performed well.

Following nonstationary analysis tests suggested by Cressie [19], we present a typical example in Fig. 5. The log-magnitude medium-frequency block is shown in Fig. 5(a). After removing linear trends, boxplots of the rows are shown in Fig. 5(b). An examination of the boxplots of Fig. 5(a) shows that they tend to follow a relatively stable pattern. A similar result is evident in the boxplots of the columns shown in Fig. 5(c). A more sophisticated test of nonstationarity is presented in the “pocket plot” of Fig. 5(d) [19]. In Fig. 5(d), along the north-south lags, we present boxplots for each row. Nonstationary behavior for a particular row is characterized by boxplots that are centered away from zero. In the plot, rows 13 and 28 show nonstationary behavior. The rest of the rows appear relatively close to zero.

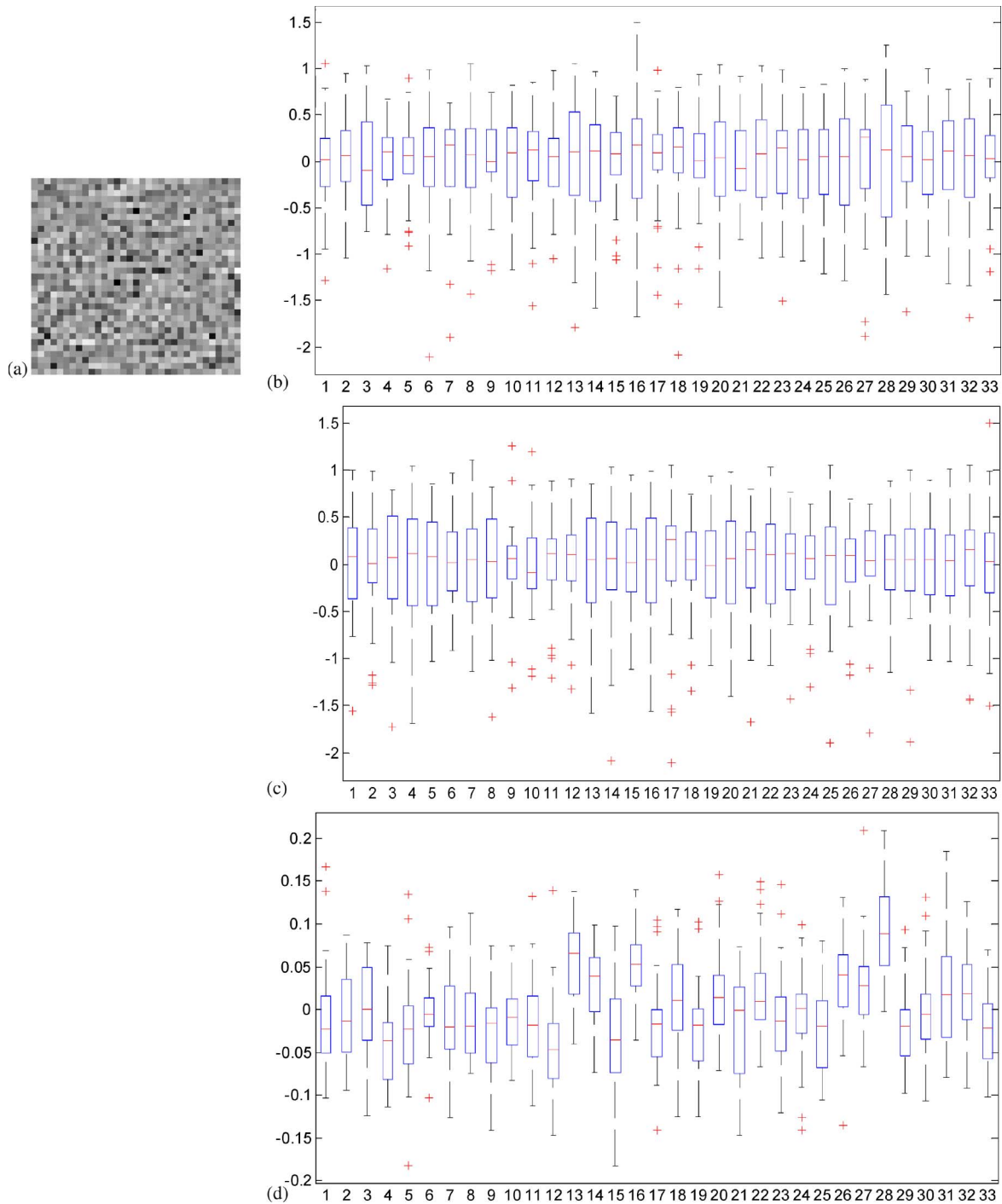


Fig. 5. Medium-frequency, log-magnitude block for testing stationarity. (a) Original image. (b) Row boxplots. (c) Column boxplots. (d) Pocket boxplot along each row for identifying nonstationary pockets in the data.

Thus, for the majority of the rows, it appears that the stationarity assumption holds.

B. Comparison of Variogram Models

In exploratory analysis for possible trends in the data, it was determined that a linear model would suffice. This decision is further supported by results that indicated that deterministic methods based on linear interpolation gave very competitive results (e.g., see Table III and later discussion in this section).

In Fig. 6, we present a comparison of various variogram models on a medium-frequency and a high-frequency block. Here, we are looking at an example of interpolating the unwrapped phase image of Fig. 6(a). Optimal, isotropic variogram models based on OK are presented in Fig. 6(b) and (c). In these examples, we note that the “unboundedness” in the ordinary variogram model indicates possible trends in the data. The use of Universal Kriging with linear trends shows much better fits in Fig. 6(d) and (e). In particular, it is clear that the variogram fits are bounded by a deterministic sill.

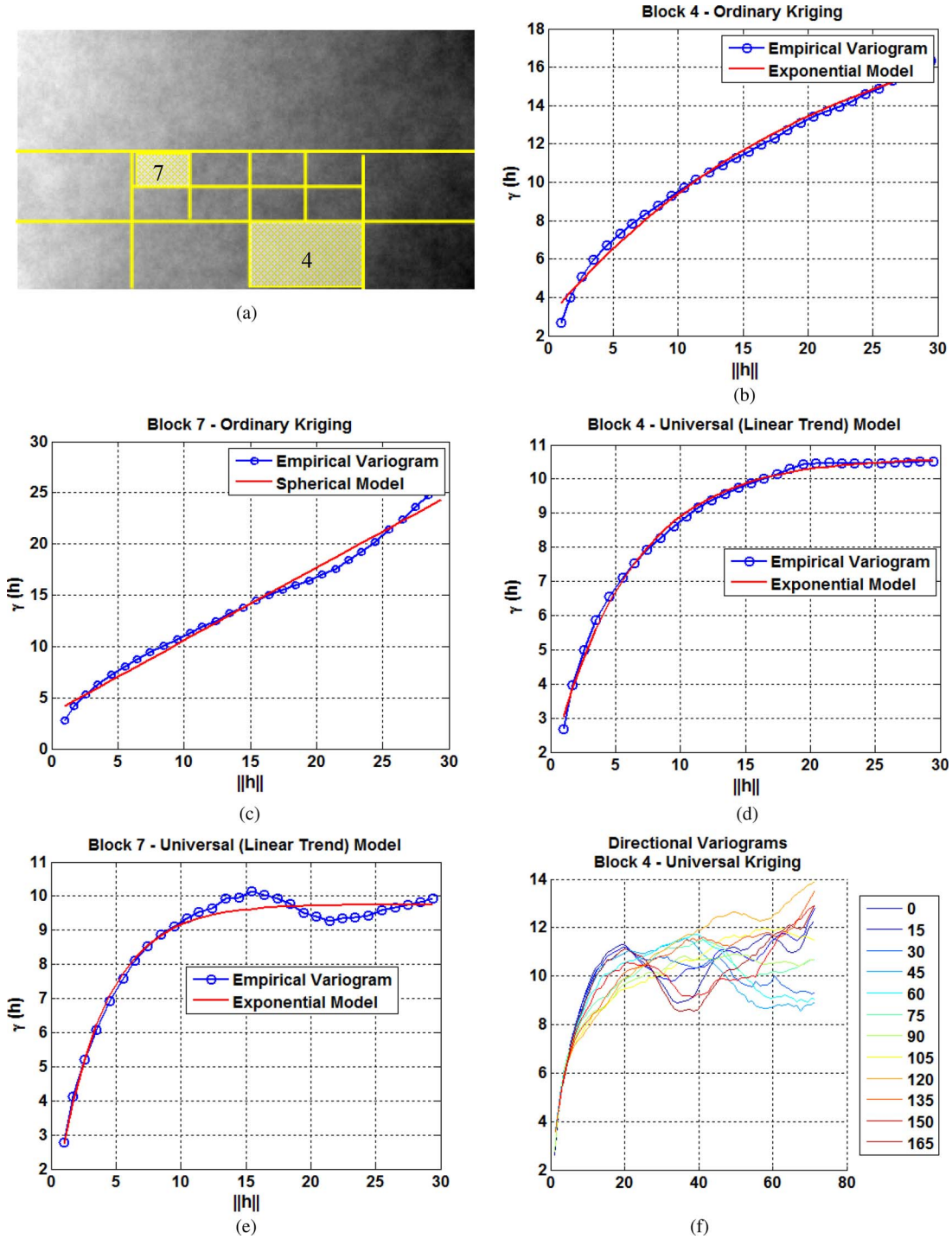


Fig. 6. Comparison of various variogram models for two specified spectral blocks of a given unwrapped phase of an image of the urban class. (a) The entire unwrapped phase and indicated blocks from which the models were derived. (b) The Ordinary Kriging empirical variogram and fitted model for Block 4. (c) The Ordinary Kriging empirical variogram and fitted model for Block 7. (d) The Universal Kriging (assuming a linear trend) empirical variogram and fitted model for Block 4. (e) The Universal Kriging empirical variogram and fitted model for Block 7. (f) The directional variograms for Block 4, indicating that no directional component has a significant correlation and an Isotropic Model is supported in this case.

While Universal Kriging appears to be much better suited for phase interpolation, it did significantly worse than OK on magnitude interpolation. Phase interpolation is limited by the need for phase unwrapping and the nonstationary characteristics of the phase. Also, we found that Universal Kriging could lead to overfitting the magnitude data. This observation is significant because most of the compression gains come from interpolating

the high-frequency magnitude blocks. As we discuss later in this section, this resulted in OK performing well when comparing image reconstruction quality to that of Universal Kriging.

The use of anisotropic models proved to be somewhat less effective. Some of the issues are demonstrated in Fig. 6(f). In the example of Fig. 6(f), note that there is no clear dominant direction. Furthermore, at larger distances, the estimates tended to

TABLE II
HIGH-FREQUENCY BLOCK RECONSTRUCTION PSNR, MAGNITUDE. SAMPLING RATES
ARE EQUAL ALONG THE HORIZONTAL AND VERTICAL DIRECTIONS

	Statistic Sample Rate	Min	1 st Quartile	Median	3 rd Quartile	Max
Ord. Isot. Kriging	1:16 ²	44.9250	50.2470	52.1638	53.3509	55.0397
	1:8 ²	46.7038	51.6753	53.7825	54.7097	56.7870
	1:4 ²	46.7038	53.4854	55.1832	55.7543	57.7496
Spline	1:16 ²	43.5644	47.8149	50.0642	51.1259	53.3444
	1:8 ²	45.8346	48.8110	50.8671	51.2437	52.9376
	1:4 ²	45.8207	50.0140	50.3334	51.6328	53.4519
Nearest	1:16 ²	41.7850	45.9392	48.2797	49.5575	51.3172
	1:8 ²	43.7956	46.6477	48.2320	49.4008	51.0215
	1:4 ²	43.8480	47.8078	48.8800	49.5472	51.3849
Linear	1:16 ²	45.7441	49.1677	51.5058	52.3860	53.7980
	1:8 ²	46.7093	50.2485	51.4099	52.5443	54.2441
	1:4 ²	47.2029	51.2519	52.2092	52.9615	54.7953

be noisier since there are fewer samples used in the estimation. On the other hand, the presence of strong, directional spatial components did lead to better fits by anisotropic models. Here, we use the term “strong” to refer to long spatial extends. For example, a long road will lead to the need for anisotropic models. Overall, though, as we shall describe later, the significant computational complexity associated with fitting anisotropic models may not be justified by marginal improvements in the results.

C. Magnitude and Phase Kriging

Based on the sampling rates that were considered and the range of the empirical variogram models, we considered fitting the variogram from two to the number of samples that ensure complete inclusion of all data points within a given spectral block. The combination of these parameters led us to perform a search for the optimal estimation parameters for Kriging reconstruction on both the magnitude and unwrapped phase data, respectively.

Table II contains nonparametric summary statistics of the high-frequency block magnitude reconstruction PSNR values over all ten images. The statistics we have chosen are the minimum, first quartile, median, third quartile, and maximum PSNR values of all reconstructions at the three high-frequency sample reduction rates and the three medium-frequency sample reduction rates. For comparison, the same statistics for the cubic spline, nearest neighbor, and linear interpolation algorithms are also included. The above results were obtained by fitting the minimum number of semivariance values up to either a radius of 25 for sample rates greater than 8; or the radial distance equal to three times the sampling rate for sample rates less than

8. The Ordinary, isotropic Kriging steps were performed using the derived max-samples from a max-distance parameter value of 25 for the high-frequency blocks and 20 for the medium-frequency blocks. Experiments on both the high and medium-frequency blocks revealed that these are the optimal parameter values. Going beyond 25 neighbors does not gain significant improvement in reconstructions. The additional computational cost is not worth an unperceivable gain in reconstruction quality.

Relative PSNR improvements obtained by using Kriging over the other interpolators for the medium-frequency blocks of the magnitude of the Fourier samples were very similar to the results of the high-frequency blocks. Not surprisingly, the PSNR values were higher for the medium-frequency blocks because of the higher sampling rates used in our approach for the data in the middle of the Fourier domain.

Similar reconstruction performance tests were done on the various phase unwrapping methods presented above. Our experimental results indicated that the PCG method shows the highest median PSNR values. The overall best reconstructions (based on the maximum achieved PSNR) were achieved using Flynn’s minimum discontinuity method. Both methods resulted in similar statistical values, and our choice again returns to the amount of unwrapping performed by each method. As noted previously, Flynn’s minimum discontinuity method produces the globally minimal phase unwrapping solution. Errors within an unwrapped surface that is represented by a smaller range of phase values will produce a smaller absolute error when the phase is rewrapped by the inverse FFT operation than an unwrapped surface with greater range in the unwrapped phase values. The PCG and Flynn method are both iterative as they solve optimization problems.

TABLE III
IMAGE RECONSTRUCTION PERFORMANCE, PHASE, AND MAGNITUDE SAMPLING

Sampling Rate	Reconstruction Method	Mean PSNR			Mean SSIM		
		Rural Images	Natural Images	Urban Images	Rural Images	Natural Images	Urban Images
S1 28.91%	Ord. Isot. Kriging	81.57	73.02	63.68	0.9114	0.8434	0.8718
	Cubic Spline	82.91	69.55	60.18	0.9033	0.7717	0.8239
	Bilinear	83.88	70.44	61.24	0.9141	0.7894	0.8384
	Nearest Neighbor	81.78	68.42	58.97	0.8893	0.7431	0.8075
S2 27.15%	Ord. Isot. Kriging	79.53	71.93	62.40	0.9019	0.8298	0.8577
	Cubic Spline	80.18	66.21	58.31	0.8857	0.7386	0.7983
	Bilinear	81.11	67.11	59.52	0.8968	0.7584	0.8158
	Nearest Neighbor	78.81	65.52	57.27	0.8631	0.7101	0.7835
S3 26.71%	Ord. Isot. Kriging	78.42	71.09	61.71	0.8952	0.8168	0.8490
	Cubic Spline	78.28	64.12	56.48	0.8717	0.7210	0.7688
	Bilinear	79.03	64.97	57.39	0.8806	0.7411	0.7837
	Nearest Neighbor	76.17	64.10	56.29	0.8333	0.7012	0.7697
S4 25.78%	Ord. Isot. Kriging	75.89	63.85	54.02	0.8565	0.7440	0.7318
	Cubic Spline	82.91	69.55	60.18	0.9033	0.7717	0.8239
	Bilinear	83.88	70.43	61.24	0.9141	0.7894	0.8384
	Nearest Neighbor	81.78	64.10	58.97	0.8893	0.7431	0.8075
S5 24.02%	Ord. Isot. Kriging	74.90	63.24	53.56	0.8511	0.7319	0.7178
	Cubic Spline	80.18	66.21	58.31	0.8857	0.7386	0.7983
	Bilinear	81.11	67.11	59.52	0.8968	0.7584	0.8158
	Nearest Neighbor	78.81	65.52	57.27	0.8631	0.7101	0.7835
S6 23.58%	Ord. Isot. Kriging	74.22	62.78	53.31	0.8461	0.7213	0.7110
	Cubic Spline	78.28	64.12	56.48	0.8717	0.7210	0.7688
	Bilinear	79.03	64.97	57.39	0.8806	0.7411	0.7837
	Nearest Neighbor	76.17	68.42	56.29	0.8333	0.7012	0.7697
S7 11.72%	Ord. Isot. Kriging	68.75	56.72	47.43	0.7620	0.6250	0.5302
	Cubic Spline	69.40	56.02	46.11	0.7617	0.5898	0.4658
	Bilinear	69.69	56.40	46.50	0.7724	0.6085	0.4823
	Nearest Neighbor	68.16	55.39	45.46	0.7434	0.5774	0.4389
S8 9.96%	Ord. Isot. Kriging	68.31	56.37	47.21	0.7586	0.6231	0.5176
	Cubic Spline	69.31	56.01	46.16	0.7618	0.5945	0.4688
	Bilinear	69.63	56.44	46.65	0.7733	0.6156	0.4866
	Nearest Neighbor	68.04	55.33	45.53	0.7456	0.5879	0.4472
S9 9.52%	Ord. Isot. Kriging	67.98	56.09	47.10	0.7558	0.6179	0.5136
	Cubic Spline	69.33	55.81	46.37	0.7643	0.5946	0.4687
	Bilinear	69.63	56.28	46.79	0.7740	0.6176	0.4852
	Nearest Neighbor	67.53	54.99	45.52	0.7399	0.5895	0.4489
S10 8.20%	Ord. Isot. Kriging	67.16	55.28	45.96	0.7613	0.6379	0.4709
	Cubic Spline	66.85	54.21	45.01	0.7457	0.6072	0.4350
	Bilinear	67.09	54.53	45.32	0.7544	0.6339	0.4470
	Nearest Neighbor	66.30	53.57	44.57	0.7417	0.5787	0.4156
S11 6.45%	Ord. Isot. Kriging	67.26	55.29	46.15	0.7705	0.6482	0.4767
	Cubic Spline	66.93	54.24	45.10	0.7479	0.6180	0.4399
	Bilinear	67.20	54.55	45.49	0.7579	0.6323	0.4527
	Nearest Neighbor	66.00	53.70	44.60	0.7405	0.5949	0.4221
S12 6.01%	Ord. Isot. Kriging	67.07	55.05	46.09	0.7699	0.6463	0.4739
	Cubic Spline	67.18	53.92	45.40	0.7532	0.6192	0.4417
	Bilinear	67.40	54.16	45.74	0.7614	0.6193	0.4540
	Nearest Neighbor	65.59	53.38	44.63	0.7395	0.5984	0.4270

D. Image Reconstruction Comparisons

We provide comparative image reconstruction results based on Kriging, bilinear, cubic spline, and nearest neighbor interpolation. Tables III and IV summarize the reconstructed image quality for each image class in terms of average PSNR

and SSIM values at each sampling rate. In each case, the corresponding phase and magnitude sampling geometry can be found in Table I. Magnitude-only interpolation results are presented in the upper part of the table for sampling geometries S1–S3. Combined magnitude and phase interpolation results

TABLE IV
IMAGE RECONSTRUCTION PERFORMANCE, COMPARING ISOTROPIC AND ANISOTROPIC MODELS USING ORDINARY AND UNIVERSAL KRIGING

Sampling Rate	Reconstruction Method	Mean PSNR			Mean SSIM		
		Rural Images	Natural Images	Urban Images	Rural Images	Natural Images	Urban Images
S1 28.91%	Ordinary Isotropic	81.57	73.02	63.68	0.9114	0.8434	0.8718
	Ord. Anisotropic	80.37	71.75	62.53	0.9144	0.8181	0.8553
	Universal Isotropic	78.75	69.98	61.28	0.8883	0.7855	0.8388
	Univ. Anisotropic	78.49	69.85	61.22	0.8860	0.7829	0.8380
S2 27.15%	Ordinary Isotropic	79.53	71.93	62.40	0.9019	0.8298	0.8577
	Ord. Anisotropic	77.19	70.08	61.09	0.8998	0.8058	0.8394
	Universal Isotropic	70.30	67.52	58.46	0.8007	0.7578	0.8003
	Univ. Anisotropic	70.38	67.34	58.24	0.7998	0.7537	0.7968
S3 26.71%	Ordinary Isotropic	78.42	71.09	61.71	0.8952	0.8168	0.8490
	Ord. Anisotropic	75.73	69.44	60.67	0.8935	0.7944	0.8352
	Universal Isotropic	70.39	64.18	55.21	0.7937	0.7031	0.7559
	Univ. Anisotropic	70.48	64.28	55.05	0.7951	0.7046	0.7536
S4 25.78%	Ordinary Isotropic	75.89	63.85	54.02	0.8565	0.7440	0.7318
	Ord. Anisotropic	75.04	63.35	54.58	0.8730	0.7507	0.7498
	Universal Isotropic	75.97	64.86	54.98	0.8767	0.7538	0.7444
	Univ. Anisotropic	75.28	63.86	54.31	0.8691	0.7330	0.7351
S5 24.02%	Ordinary Isotropic	74.90	63.24	53.56	0.8511	0.7319	0.7178
	Ord. Anisotropic	73.26	62.74	53.85	0.8611	0.7413	0.7367
	Universal Isotropic	73.87	64.04	54.46	0.8640	0.7428	0.7290
	Univ. Anisotropic	73.03	63.13	54.06	0.8478	0.7209	0.7176
S6 23.58%	Ordinary Isotropic	74.22	62.78	53.31	0.8461	0.7213	0.7110
	Ord. Anisotropic	72.05	62.26	53.05	0.8767	0.7538	0.7444
	Universal Isotropic	72.53	63.32	53.10	0.8478	0.7180	0.7192
	Univ. Anisotropic	72.45	62.30	53.13	0.8419	0.6949	0.7097
S7 11.72%	Ordinary Isotropic	68.75	56.72	47.43	0.7620	0.6250	0.5302
	Ord. Anisotropic	67.32	57.00	47.23	0.7627	0.6313	0.5075
	Universal Isotropic	67.19	56.77	46.95	0.7457	0.6148	0.4952
	Univ. Anisotropic	66.99	56.63	46.87	0.7386	0.5880	0.4814
S8 9.96%	Ordinary Isotropic	68.31	56.37	47.21	0.7586	0.6231	0.5176
	Ord. Anisotropic	67.19	56.90	47.18	0.7680	0.6356	0.5017
	Universal Isotropic	63.68	56.44	46.58	0.6788	0.6128	0.4822
	Univ. Anisotropic	63.74	56.31	46.44	0.6749	0.5857	0.4663
S9 9.52%	Ordinary Isotropic	67.98	56.09	47.10	0.7558	0.6179	0.5136
	Ord. Anisotropic	67.27	56.72	47.16	0.7723	0.6284	0.5006
	Universal Isotropic	64.06	55.27	45.74	0.6944	0.5871	0.4690
	Univ. Anisotropic	64.11	55.28	45.59	0.6880	0.5564	0.4519
S10 8.20%	Ordinary Isotropic	67.16	55.28	45.96	0.7613	0.6379	0.4709
	Ord. Anisotropic	65.38	54.60	45.44	0.7434	0.6197	0.4410
	Universal Isotropic	65.06	54.30	45.18	0.7232	0.5959	0.4273
	Univ. Anisotropic	65.00	54.26	45.10	0.7168	0.5699	0.4126
S11 6.45%	Ordinary Isotropic	67.26	55.29	46.15	0.7705	0.6482	0.4767
	Ord. Anisotropic	65.65	54.82	45.62	0.7539	0.6335	0.4467
	Universal Isotropic	62.43	54.47	45.07	0.6792	0.6085	0.4271
	Univ. Anisotropic	62.40	54.43	44.94	0.6730	0.5798	0.4105
S12 6.01%	Ordinary Isotropic	67.07	55.05	46.09	0.7699	0.6463	0.4739
	Ord. Anisotropic	65.81	54.59	45.64	0.7584	0.6288	0.4466
	Universal Isotropic	62.61	53.48	44.34	0.6920	0.5907	0.4201
	Univ. Anisotropic	62.58	53.56	44.21	0.6854	0.5625	0.4033

are given in the lower part of the table for sampling geometries S4–S12.

In terms of SSIM, we consider reconstruction results to be excellent if they achieve values above 0.75 (maximum = 1.0, see [20]). One of the most exciting results is that we can achieve

excellent reconstructions for rural images using just 6.01% of the original FFT samples by sampling geometry S12. For this geometry, for the high-frequency blocks, only one out of 64 phase samples are kept. The caption in Table I provides more details for S12. Ordinary, anisotropic Kriging provides the best

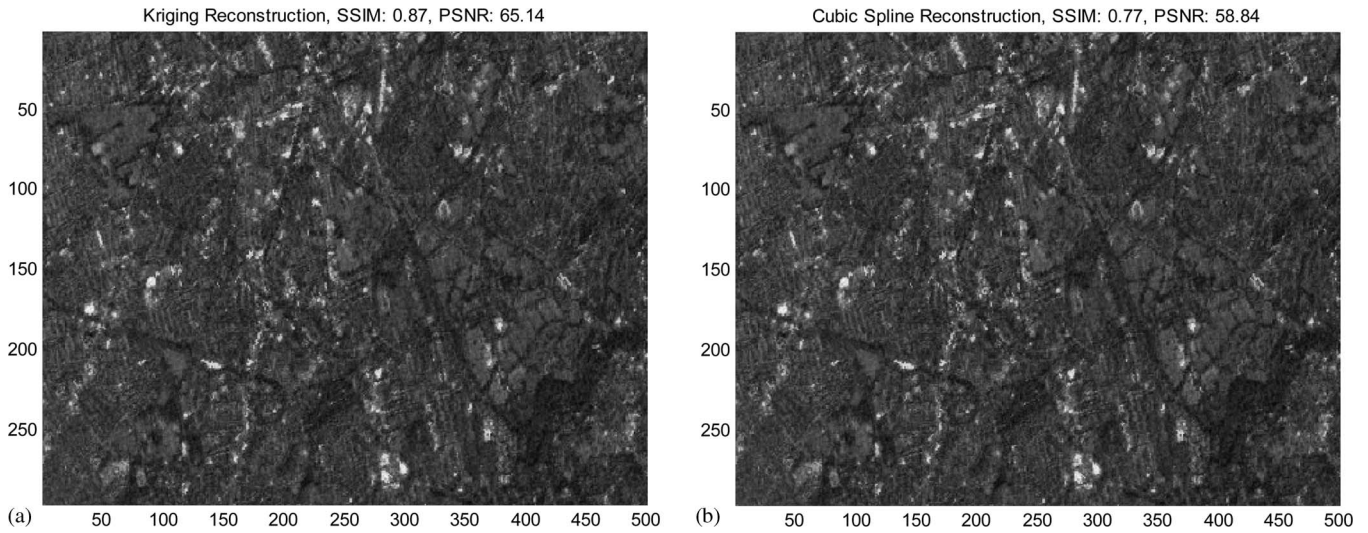


Fig. 7. Urban image reconstruction example based on S3 (see Table I). The top reconstruction is a sample urban scene in which the magnitude downsampling rate was eight in the middle frequency blocks in each dimension and 16 in the outer frequency blocks in each dimension using the Kriging interpolator for the magnitude coefficients. (b) Same image using Spline interpolation.

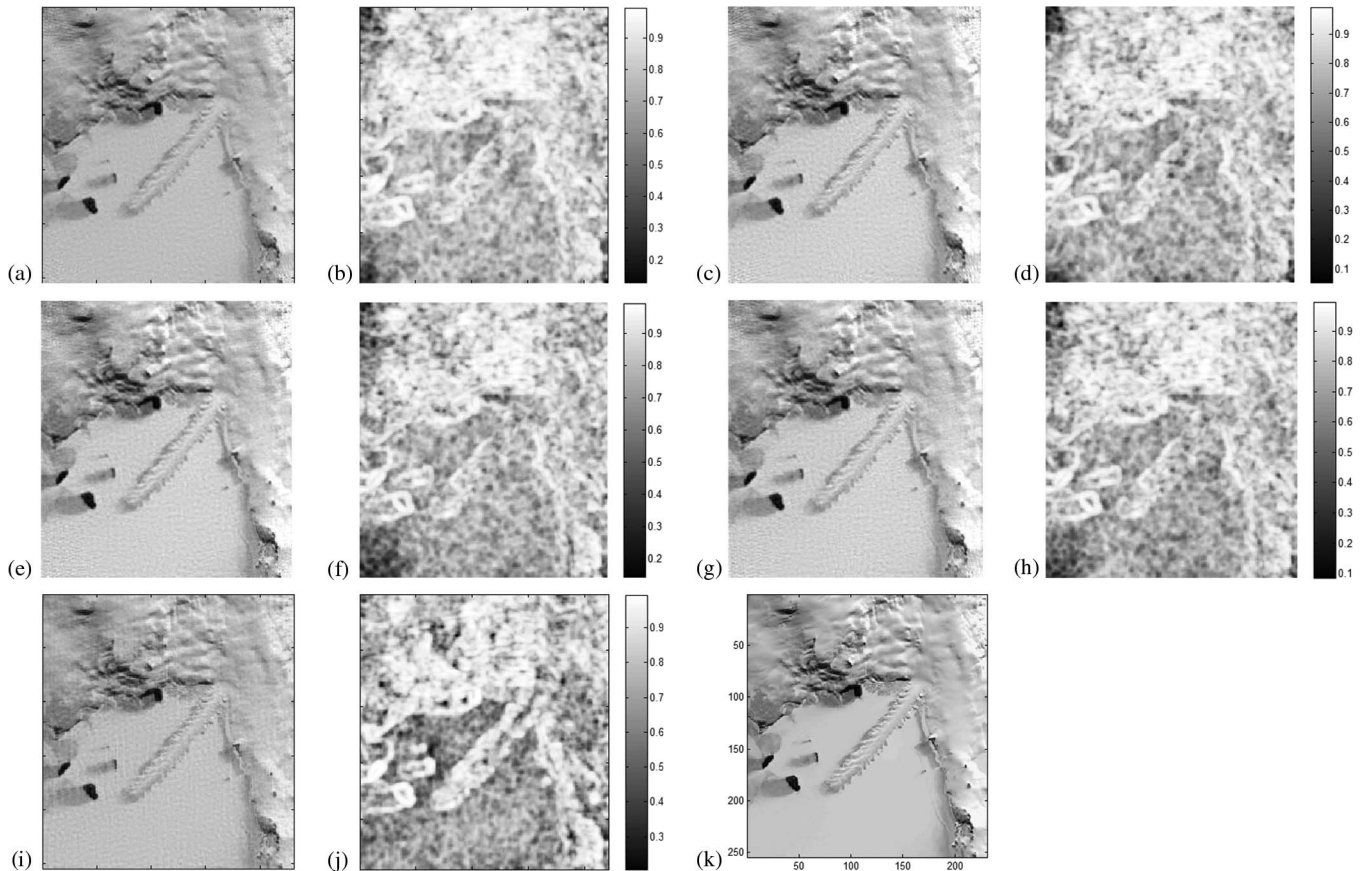


Fig. 8. Natural image reconstruction example based on S5 (see Table I). (a) Ordinary Kriging with Isotropic Model reconstructed image (PSNR = 68.42 dB). (b) SSIM image (mean value = 0.8018). (c) Ordinary Kriging with Anisotropic Model reconstructed image (PSNR = 67.29 dB). (d) SSIM image (mean value = 0.7970). (e) Universal Kriging with Isotropic Model reconstructed image (PSNR = 68.24 dB). (f) SSIM image (mean value = 0.7966). (g) Universal Kriging with Anisotropic Model reconstructed image (PSNR = 67.78 dB). (h) SSIM image (mean value = 0.7882). (i) Bicubic interpolation reconstructed image (PSNR = 69.02 dB). (j) SSIM image quality map for bicubic interpolation reconstructed image (mean value = 0.7670). (k) Original Image for comparison.

mean-SSIM results for this case. Same goes for S11 at just 6.45% and S10 at just 8.2% of the 2-D FFT samples.

For natural images, we do not get excellent reconstructions until we increase the sampling rate to 24.02% (S5 sampling

geometry). For the S5 sampling geometry, it is interesting to note that bilinear interpolation outperformed all other methods.

Among Kriging methods, Universal Kriging with isotropic modeling has generally given better results for the S4 (25.78%)

and S5 (24.02%) geometries. For these geometries, in terms of image quality, Universal Kriging with isotropic modeling gives excellent performance. The very best reconstructions are given by OK interpolation for reconstructions based on magnitude-only interpolation (S1–S3 for 26.71% to 28.91%). Bilinear interpolation provides the best results at the lower sampling rates associated with S4 and S5. For urban images, excellent reconstructions can be obtained with just 23.58% of the samples (S6 sampling geometry). Again, OK with isotropic modeling dominates over other reconstruction methods for magnitude-only interpolation while bilinear dominates when phase interpolation is added. Anisotropic Kriging methods did give better reconstructions for some geometries (e.g., S6 and S9). It is interesting to note that in the cases where Universal and anisotropic Kriging outperformed Ordinary, isotropic Kriging, bilinear interpolation yielded the best results. In fact, in all these cases, Bilinear interpolation did better than Kriging methods.

Fig. 7 shows the reconstructed urban scene for the S3 sampling geometry (see Table I). The reconstruction in (a) was achieved using the Kriging interpolator for magnitude and used the original phase spectra in the reconstruction. Note the improvement in SSIM (+9.64%) and PSNR (+6.3 dB) over the cubic spline interpolated reconstruction in (b).

Fig. 8 shows a reconstructed natural image scene for the S5 sampling geometry (see Table I). In terms of PSNR, OK with isotropic modeling and Bicubic interpolation gave similar performance (68.4 dB versus 69.0 dB). On the other hand, the average SSIM was better for OK (0.80 versus 0.77). A careful comparison of the SSIM quality maps in Fig. 8 (b) and (j) shows significant differences. For the Bicubic reconstruction, the SSIM quality maps seem to be highly correlated to the input image. This implies that the Bicubic reconstruction does not provide a model that works uniformly over different image structures. Kriging reconstructions do better in this respect. The Kriging SSIM maps of Fig. 8 do not have strong correlations to the input image. Overall, it is interesting to note that OK with isotropic modeling did better than all other Kriging approaches. Universal Kriging with isotropic modeling was a close second. It is also interesting to note that anisotropic models did not perform better than the isotropic models. Spatially, we can see image structures among many different directions in the input image. This probably contributes to the fact that picking the dominant direction did not work so well.

V. CONCLUSION

In this paper, we have developed a nonstationary spectral covariance modeling technique for application to both phase and magnitude interpolation. We have developed scalable sampling geometries that also allow for independent rates for the phase and magnitude. Excellent image reconstructions are obtained using a fraction of the original FFT magnitude and phase samples. This allows the compression of remote sensing images by representing them with a fraction of the FFT coefficients.

By partitioning the frequency spectrums into independent blocks, we provide a nonstationary method that produces an effective spectral covariance model over small, intrinsically stationary regions. Theoretical variogram models were then

calculated for each block in an adaptive fashion, ensuring the selection of the best models. Using the optimal models, we were able to reconstruct the phase and magnitude spectra using stochastic or deterministic interpolation methods. Using individual reconstructions from ten images and 12 frequency blocks per image (keeping the two low-pass blocks “as is”), we were able to explore the effect of the number of samples (which is proportional to the block sample rate) used in the Kriging estimate and discovered that a relationship exists between the number of samples used in Kriging and the reconstruction accuracy.

The large number of Kriged phase blocks allowed for a quantitative comparison between phase unwrapping methods. The path following phase unwrapping algorithms result in unique phase surfaces. We have shown that some unwrapping methods result in phase surfaces that are better suited for our spectral statistical modeling approach. It was found that both the Flynn’s minimal discontinuity and both minimum norm methods (weighted multigrid and PCG) resulted in much better block reconstructions. Our decision to implement Flynn’s method was due to the fact that it generally results in a smaller range in the unwrapped values, from which localized interpolation values will result in a smaller absolute error when the inverse 2-D FFT is applied to the reconstructed magnitude and phase spectra.

For urban images, OK with isotropic modeling gave the best interpolation results at extremely low sampling rates (6.01%). This method also gave the best reconstruction results for magnitude-only interpolation for natural and urban images. Universal Kriging with linear trends and isotropic models gave excellent results for the S4 (25.78%) and S5 (24.02%) geometries.

In terms of performance and computational complexity, Ordinary, isotropic Kriging was the preferred method. It produced satisfactory results given that it was the simplest and most efficient method in terms of computational complexity. Our investigation suggests that it worked better by avoiding overfitting the magnitude spectrum data. Furthermore, compared to the best deterministic approaches, Kriging methods provided image reconstructions with more uniform quality (see Fig. 8). In contrast, the quality of reconstructions from deterministic methods appears to correlate strongly to the input image (see Fig. 8). Overall, by considering Universal Kriging with trend functions, stochastic models allow for better flexibility in the model.

The paper did not investigate lossless encoding methods. Lossless phase encoding can be used in addition to magnitude interpolation to improve the results. Phase interpolation is clearly much more challenging than magnitude interpolation. Phase unwrapping makes the phase interpolation process possible.

REFERENCES

- [1] A. V. Oppenheim and J. S. Lim, “The importance of phase in signals,” *Proc. IEEE*, vol. 69, no. 5, pp. 529–541, May 1981.
- [2] L. C. Graham, “Synthetic interferometer radar for topographic mapping,” *Proc. IEEE*, vol. 62, no. 6, pp. 763–768, Jun. 1974.
- [3] R. M. Goldstein, H. A. Zebker, and C. L. Werner, “Satellite radar interferometry: Two-dimensional phase unwrapping,” *Radio Sci.*, vol. 23, no. 4, pp. 713–720, Jul./Aug. 1988.
- [4] F. K. Li and R. M. Goldstein, “Studies of multibaseline spaceborne interferometric synthetic aperture radars,” *IEEE Trans. Geosci. Remote Sens.*, vol. 28, no. 1, pp. 88–97, Jan. 1990.

- [5] A. L. Gray and P. J. Farris-Manning, "Repeat-pass interferometry with airborne synthetic aperture radar," *IEEE Trans. Geosci. Remote Sens.*, vol. 31, no. 1, pp. 180–191, Jan. 1993.
- [6] D. Massonnet, M. Rossi, C. Carmona, F. Adragna, G. Peltzer, K. Feigl, and T. Rabaute, "The displacement field of Landers earthquake mapped by radar interferometry," *Nature*, vol. 364, no. 6433, pp. 138–142, Jul. 1993.
- [7] D. C. Ghiglia and P. H. Eichel, "High-resolution synthetic aperture radar interferometry: Technology for precise terrain elevation mapping," *DSP Multimedia Technol.*, vol. 3, pp. 1–12, 1994.
- [8] D. T. Sandell, D. Myer, R. Mellors, M. Shimada, B. Brooks, and J. Foster, "Accuracy and resolution of ALOS interferometry: Vector deformation maps of the Father's day intrusion at Kilauea," *IEEE Trans. Geosci. Remote Sens.*, vol. 46, no. 11, pp. 3524–3534, Nov. 2008.
- [9] M. Eineder, N. Adam, R. Bamler, N. Y. Martinez, and H. Breit, "Spaceborne spotlight SAR interferometry with TerraSAR-X," *IEEE Trans. Geosci. Remote Sens.*, vol. 47, no. 5, pp. 1524–1535, May 2009.
- [10] A. C. Kak and M. Slaney, *Principles of Computerized Tomographic Imaging*. Philadelphia, PA: SIAM, 2001, ch. 3.
- [11] D. E. Wahl, P. E. Eichel, D. C. Ghiglia, P. A. Thompson, and C. V. Jakowatz, *Spotlight-Mode Synthetic Aperture Radar: A Signal Processing Approach*. New York: Springer-Verlag, 1996.
- [12] S. C. Park, M. K. Park, and M. G. Kang, "Super-resolution image reconstruction: A technical overview," *IEEE Signal Process. Mag.*, vol. 20, no. 3, pp. 21–36, May 2003.
- [13] M. Unser, "Splines: A perfect fit for signal processing," *IEEE Signal Process. Mag.*, vol. 16, no. 6, pp. 22–38, Nov. 1999.
- [14] Purdue University Laboratory for Applications of Remote Sensing, 2006, Image sv010813_ARC_F106_1m. Retrieved April 27, 2009 from ITD Spectral Visions Multispectral Image Database. [Online]. Available: www.lars.purdue.edu/home/image_data/spectral_vision_data.html
- [15] Purdue University Laboratory for Applications of Remote Sensing, 2006, Image sv010706_FPS_south_1m. Retrieved January 16, 2009 from ITD Spectral Visions Multispectral Image Database. [Online]. Available: http://www.lars.purdue.edu/home/image_data/spectral_vision_data.html
- [16] NASA/GSFC/METI/ERSDAC/JAROS, and U.S./Japan ASTER Team, Retrieved January 16, 2009 from ASTER Project Image Database, London, U.K., 2001. [Online]. Available: <http://asterweb.jpl.nasa.gov/gallery/images/london-final.jpg>
- [17] NASA/GSFC/LaRC/JPL, MISR Team, The Grand Canyon. Retrieved March 3, 2009 from MISR Image Gallery, 2000. [Online]. Available: <http://photojournal.jpl.nasa.gov/catalog/PIA03402>
- [18] V. Murray, P. Rodriguez, and M. S. Pattichis, "Multi-scale AM-FM demodulation and reconstruction methods with improved accuracy," *IEEE Trans. Image Process.*, vol. 19, no. 5, pp. 1138–1152, May 2010.
- [19] N. A. Cressie, *Statistics for Spatial Data*. New York: Wiley, 1993, revised edition.
- [20] Z. Wang, A. C. Bovik, H. R. Sheikh, and E. P. Simoncelli, "Image quality assessment: From error visibility to structural similarity," *IEEE Trans. Image Process.*, vol. 3, no. 4, pp. 600–612, Apr. 2004.
- [21] B. Girod, "What's wrong with mean-squared error?," in *Digital Images and Human Vision*, A. B. Watson, Ed. Cambridge, MA: MIT Press, 1993, pp. 207–220.
- [22] N. Cressie, "The origins of Kriging," *Math. Geol.*, vol. 22, no. 3, pp. 239–252, Apr. 1990.
- [23] K. Cheng, H. Yeh, and C. Tsai, "An anisotropic modeling approach for remote sensing image rectification," *Remote Sens. Environ.*, vol. 73, no. 1, pp. 46–54, Jul. 2000.
- [24] P. S. Kanaroglou, N. A. Soulakellis, and N. I. Sifakis, "Improvement of satellite derived pollution maps with the use of a geostatistical interpolation method," *J. Geograph. Syst.*, vol. 4, no. 2, pp. 193–208, Jun. 2002.
- [25] R. E. Rossi, J. L. Dungan, and L. R. Beck, "Kriging in the shadows—Geostatistical interpolation for remote sensing," *Remote Sens. Environ.*, vol. 49, no. 1, pp. 32–40, Jul. 1994.
- [26] A. Ferretti, C. Prati, and F. Rocca, "Permanent scatterers in SAR interferometry," *IEEE Trans. Geosci. Remote Sens.*, vol. 39, no. 1, pp. 8–20, Jan. 2001.
- [27] T. Blaschke, "Object-based contextual image classification build on image segmentation," in *Proc. IEEE Workshop Adv. Tech. Anal. Remotely Sens. Data*, Oct. 2004, pp. 113–119.
- [28] J. Djamdji and A. Bijaoui, "Disparity analysis: A wavelet transform approach," *IEEE Trans. Geosci. Remote Sens.*, vol. 33, no. 1, pp. 67–76, Jan. 1995.
- [29] J. R. Carr, "Spectral and textural classification of single and multiple band digital images," *Comput. Geosci.*, vol. 22, no. 8, pp. 1063–1079, Oct. 1990.
- [30] P. M. Atkinson, E. Pardo-Iguzquiza, and M. Chica-Olmo, "Downscaling cokriging for super-resolution mapping of continua in remotely sensed images," *IEEE Trans. Geosci. Remote Sens.*, vol. 46, no. 2, pp. 573–580, Feb. 2008.
- [31] M. P. Foster and A. N. Evans, "An evaluation of interpolation techniques for reconstructing ionospheric TEC maps," *IEEE Trans. Geosci. Remote Sens.*, vol. 46, no. 7, pp. 2153–2164, Jul. 2008.
- [32] B. Saulquin, F. Gohin, and R. Garrello, "Regional objective analysis for merging high-resolution MERIS, MODIS/Aqua, and SeaWiFS Chlorophyll—A data from 1998 to 2008 on the European Atlantic Shelf," *IEEE Trans. Geosci. Remote Sens.*, vol. 49, no. 1, pp. 143–154, Jan. 2011.
- [33] A. Abrardo, M. Barni, E. Magli, and F. Nencini, "Error-resilient and low-complexity onboard lossless compression of hyperspectral images by means of distributed source coding," *IEEE Trans. Geosci. Remote Sens.*, vol. 48, no. 4, pp. 1892–1904, Apr. 2010.
- [34] I. Blanes and J. Serra-Sagrístà, "Cost and scalability improvements to the Karhunen-Loève transform for remote-sensing image coding," *IEEE Trans. Geosci. Remote Sens.*, vol. 48, no. 9, pp. 2854–2863, Sep. 2010.
- [35] I. Blanes and J. Serra-Sagrístà, "Pairwise orthogonal transform for spectral image coding," *IEEE Trans. Geosci. Remote Sens.*, vol. 49, no. 3, pp. 961–972, Mar. 2011.
- [36] X. X. Zhu and R. Bamler, "Tomographic SAR inversion by L_1 -norm regularization—The compressive sensing approach," *IEEE Trans. Geosci. Remote Sens.*, vol. 48, no. 10, pp. 3839–3846, Oct. 2010.
- [37] A. Moccia and A. Renga, "Spatial resolution of bistatic synthetic aperture radar: Impact of acquisition geometry on imaging performance," *IEEE Trans. Geosci. Remote Sens.*, vol. 49, no. 10, pp. 3487–3503, Oct. 2011.
- [38] S. G. Mallat and Z. Zhang, "Matching pursuits with time-frequency dictionaries," *IEEE Trans. Signal Process.*, vol. 41, no. 12, pp. 3397–3415, Dec. 1993.
- [39] E. J. Pebesma, *Gstat User's Manual*, Aug. 1, 2001. [Online]. Available: <http://www.gstat.org/manual.html>
- [40] D. C. Ghiglia and M. D. Pritt, *Two-Dimensional Phase Unwrapping: Theory, Algorithms, and Software*. New York: Wiley, 1998.
- [41] M. W. Roth, "Phase unwrapping for interferometric SAR by the least-error path," Johns Hopkins Univ. Appl. Phys. Lab., Laurel, MD, 1995, Tech. Rep.
- [42] T. J. Flynn, "Two-dimensional phase unwrapping with minimum weighted discontinuity," *J. Opt. Soc. Amer. A*, vol. 14, no. 10, pp. 2692–2701, Oct. 1997.



Oliver Jeromin (S'08–M'09) received the B.S.E.E. degree from the Illinois Institute of Technology, Chicago, and the B.A. degree in Liberal Arts from Wheaton College, Wheaton, IL, in 2002. He received the M.S.E.E. and Ph.D. degrees in electrical engineering from the University of New Mexico, Albuquerque with an emphasis on image processing in 2005 and 2010, respectively.

He served as a member of the Embedded Radar Processing Group at Sandia National Laboratories, Albuquerque, NM, where he assisted in the development and fielding of synthetic aperture radar systems. He is currently a Systems Engineer at Gentex Corporation in Zeeland, MI and is developing computer vision-based driver assist technology for the automotive industry.



Marios S. Pattichis (M'99–SM'06) received the B.Sc. (high honors and special honors) degree in computer sciences and the B.A. (high honors) degree in mathematics in 1991, the M.S. degree in electrical engineering in 1993, and the Ph.D. degree in computer engineering in 1998 from the University of Texas at Austin.

He is currently an Associate Professor in the Department of Electrical and Computer Engineering, University of New Mexico (UNM), Albuquerque.

His current research interests include mathematical models for digital image, and video processing and communications, dynamically reconfigurable computer architectures, and applications in biomedical and space imaging.

Dr. Pattichis is an Associate Editor of the IEEE TRANSACTIONS ON IMAGE PROCESSING. He was the General Chair of the 2008 IEEE Southwest Symposium on Image Analysis and Interpretation. At UNM, he received the 2004 ECE Distinguished Teaching Award and the 2006 School of Engineering Harrison Faculty Recognition Award.